Brodogradnja Volume 77 Number 2 (2026) 77201

journal homepage: www.brodogradnja.fsb.hr

Brodogradnja

An International Journal of Naval Architecture and Ocean Engineering for Research and Development

Design of an adaptive PI speed controller for FOC-driven underwater thrusters

Kaicheng Shen[1], Caoyang Yu[1], Jinrong Zheng[2], He Zhang[3], Xianbo Xiang[2], Lian Lian[1]*

[1] *State Key Laboratory of Submarine Geoscience; Key Laboratory of Polar Ecosystem and Climate Change, Ministry of Education; Shanghai Key Laboratory of Polar Life and Environment Sciences; and School of Oceanography, Shanghai Jiao Tong University, Shanghai 200030, China*

[2] *School of Naval Architecture and Ocean Engineering, Huazhong University of Science and Technology, Wuhan 430074, China*

[3] *China Ship Research and Development Academy, Beijing 100101, China*

ARTICLE INFO

Keywords:
Underwater thruster
Thruster control
Field-oriented control
Adaptive PI control

ABSTRACT

Underwater thrusters are the primary actuators in marine vehicles. The thruster drive and control methods for these thrusters considerably influence their dynamic response, accuracy, and efficiency. This study reviewed the structure of field-oriented control (FOC) and six-step commutation (SSC)–driven thrusters, comparing their advantages and disadvantages in underwater applications. Considering the dynamic performance of open-loop SSC, the precision of closed-loop SSC, and the energy efficiency of FOC, an adaptive proportional–integral (API) speed controller was introduced for FOC-driven underwater thrusters, which demonstrated superior performance in underwater conditions. Simulations were conducted to reveal the performance differences between FOC- and SSC-driven underwater thrusters and the advantages of the designed API controller in FOC-driven systems. FOC with a conventional PI speed controller exhibited a chattering-free steady state and 22.9% higher energy efficiency than the closed-loop SSC, and the API-based FOC showed improved step signal response and a 25.9% increase in amplitude bandwidth compared with conventional PI and integral–separated PI control. Furthermore, the API controller avoided speed chattering at low speed and displayed lower steady-state error than the conventional PI controller. These results support the conclusions of the higher bandwidth and overshoot avoidance of API and the higher energy efficiency of the FOC-driven motor.

1. Introduction

In recent decades, marine vehicles have played a crucial role in exploring and developing marine resources. The underwater thruster, the most essential actuator of these vehicles, often exhibits discrepancies between the commanded and actual thrusts owing to its inherent characteristics. For instance, the time-delay characteristic can hinder the thruster's ability to respond dynamically to thrust changes [1], whereas the saturation characteristic imposes an upper limit on the thruster's output [2]. Low-thrust commands usually do not work owing to the dead-zone characteristic [3,4]. Additionally, designing to reduce consumption, such as wind-assisted ship propulsion [5] and thrust optimization, is a hot topic [6]. These issues pose considerable challenges to marine control system design, leading several researchers to compensate for control errors at

* Corresponding author.
E-mail address: yucaoyang@sjtu.edu.cn

https://doi.org/10.21278/brod77201

Received 14 April 2025; Received in revised form 7 September 2025; Accepted 24 September 2025
Available online 10 October 2025
ISSN 0007-215X; eISSN 1845-5859

both the kinematic and dynamic levels [7, 8]. However, further study of the thruster itself is necessary to mitigate these constraints.

A brushless direct current (BLDC) electric motor is a common type of underwater motor that drives the underwater propeller's rotation [9, 10]. Six-step commutation (SSC) is a conventional method for driving BLDC motors [11, 12] and offers the advantages of low control complexity and high processing speed [13]. The basic SSC structure is an open-loop controller for rotational speed, eliminating the need for speed and current sensors in the motor armature. The relationship between motor voltage and rotational speed is used to generate voltage commands to control underwater thrusters. Nonetheless, at the same input voltage, the fluid velocity and angle of attack substantially affect the output thrust [14, 15], and the scale effect weakens the thrust [16]. Therefore, a rotational speed sensor is often added to achieve closed-loop thrust control [17]. In this study, open-loop and closed-loop SSC-driven underwater thrusters were compared to highlight their characteristics.

The commutation frequency in SSC is proportional to the rotational speed, resulting in high-frequency torque pulsation. Moreover, the lack of closed-loop current control in SSC results in higher energy consumption for underwater thrusters. Field-oriented control (FOC) is a more advanced method than SSC for driving BLDC motors. FOC employs space-vector pulse-width modulation (SVPWM) and coordinate transformation to synthesize an oriented magnetic field and precisely control the torque [18]. In addition, FOC provides a quieter commutation scheme than SSC control [19]. FOC has been successfully applied to underwater thrusters, offering several advantages in terms of time-delay, saturation, and dead-zone characteristics. For instance, Widy et al. demonstrated that FOC enables accurate motor control at low speeds, enhancing orientation accuracy [20]. In terms of time delay, FOC outperforms closed-loop SSC control. Regarding the saturation characteristic, the FOC-driven thruster can produce a higher thrust within the same power limitations owing to the higher energy efficiency. Apart from the FOC controller, other advanced methods such as direct torque control (DTC) are available to achieve high accuracy and efficiency. The performance comparison of SSC, FOC, and DTC reflects their respective advantages [21], but FOC is widely used.

Two closed-loop control systems are present in the FOC speed controller: the current control loop and the speed control loop. Many novel control methods based on FOC have achieved higher torque and rotational speed outputs for the current control loop. The maximum torque per ampere controller increases the torque output of the motor at the same current [22]. In contrast, the maximum rotational speed at the same magnetic flux linkage of the motor is improved by the flux weakening strategy [23]. However, the FOC controller requires a rotational speed sensor, which is disadvantageous compared with the open-loop SSC controller. Based on current observations, Paolucci et al. presented a novel polarity identification technique that exploits a high-frequency injection control to estimate thrust and torque without sensors [24]. For the speed control loop, conventional methods include proportional–integral–derivative (PID) and proportional–integral (PI) control. Furthermore, several improved control methods based on the speed loop have been introduced. Zhao et al. proposed a fuzzy-PID controller to augment the FOC adaptability and robustness [25]. Nicola et al. presented a linear adaptive disturbance rejection controller to achieve a speed closed loop and good dynamic response [26]. However, there are several challenges in speed control for underwater thrusters include: 1) Through both simulations and experiments, it has been observed that conventional PI controllers perform well only within specific speed ranges and often exhibit overshoot or undershoot outside these ranges; 2) Although advanced controllers such as those in [25, 26] improve accuracy and stability under step-load disturbances, their performance on underwater thrusters, specifically under the quadratic relationship between torque and speed characteristic of propellers [27], remains uncertain; 3) The velocity controller of underwater vehicles (e.g., [28]) may impose high bandwidth requirements on the thruster's speed controller—a aspect that has rarely been compared across different controllers. Thus, a new speed control strategy is necessary to address these issues. Considering that the speed–torque characteristics of underwater thrusters are similar to the surge–hydrodynamic attributes of vehicles, an adaptive integral terminal sliding mode controller (AITSMC) used for surge speed control [29] was employed in this study for propeller rotational speed control to enable a comparative evaluation with the proposed method.

Based on a review and comparison of FOC and SSC, an adaptive proportional–integral (API) speed controller for FOC-driven underwater thrusters was proposed and validated via simulations and experiments to establish a precise and efficient thruster control method suitable for underwater conditions. The following results were obtained: 1) The API speed controller demonstrated superior dynamic response compared with the conventional proportional–integral (PI) controller and AITSMC. 2) The API controller showed consistent step responses, outperforming both PI and integral–separated PI (ISPI) controllers and AITSMC. 3) Speed chattering was minimized at low speeds with the API controller. 4) FOC-driven thrusters exhibited higher energy efficiency and better accuracy than open-loop SSC-driven thrusters and superior dynamic performance than closed-loop SSC-driven thrusters.

The rest of the paper is organized as follows: In Section 2, the structures of FOC- and SSC-driven thrusters are reviewed, and their advantages and disadvantages in underwater applications are compared. Section 3 presents the principles and equations of the API controller for FOC speed control. Numerical simulations and experiments are described in Sections 4 and 5, respectively. Finally, Section 6 concludes the paper.

2. FOC- and SSC-driven thrusters

Typical SSC and FOC structures were compared. In addition, the performances of open-loop SSC, closed-loop SSC, and FOC were compared.

2.1 Open-loop SSC structure

The open-loop SSC driver is a standard thruster driver for small-sized marine vehicles. As illustrated in Fig. 1, the control input is a pulse-width modulation (PWM) signal that directly controls the bus voltage V_{bus}. The inverter comprises six metal oxide semiconductor field-effect transistors or insulated gate bipolar transistors and generates six conduction modes with six distinct magnetic field orientations. The inverter control table selects the appropriate voltages U_a, U_b, and U_c from six fixed voltage combinations based on the rotor position. Table 1 presents an inverter control table. When the motor rotates clockwise, the magnetic field orientation corresponds to the response of six rotor phases, and V_{bus} estimates the torque. Subsequently, the phase detector determines the approximate phase of the thruster rotor based on the back-electromotive force and selects the corresponding conduction mode from the inverter control table.

Table 1 Inverter control table

Phase	U_a	U_b	U_c
–120°	$V_{\text{bus}}/2$	$-V_{\text{bus}}/2$	0
–180°	0	$-V_{\text{bus}}/2$	$V_{\text{bus}}/2$
120°	$-V_{\text{bus}}/2$	0	$V_{\text{bus}}/2$
60°	$-V_{\text{bus}}/2$	$V_{\text{bus}}/2$	0
0°	0	$V_{\text{bus}}/2$	$-V_{\text{bus}}/2$
–60°	$V_{\text{bus}}/2$	0	$-V_{\text{bus}}/2$

Higher torque results in faster speed. For underwater thrusters, a mapping exists among V_{bus}, rotational speed, and thrust. A common strategy for thrust control involves converting the thrust command to a voltage command and inputting it into the open-loop SSC structure.

The open-loop SSC structure has several advantages as well as disadvantages:

- Because of the concise structure, it is easy to manufacture, requires no parameter tuning, and can be applied to almost any three-phase BLDC motor.
- The open-loop structure can lead to thrust discrepancies under external disturbances and different surge speeds.

– The SSC structure consumes more energy, posing a challenge to extending the life of the marine vehicle battery.

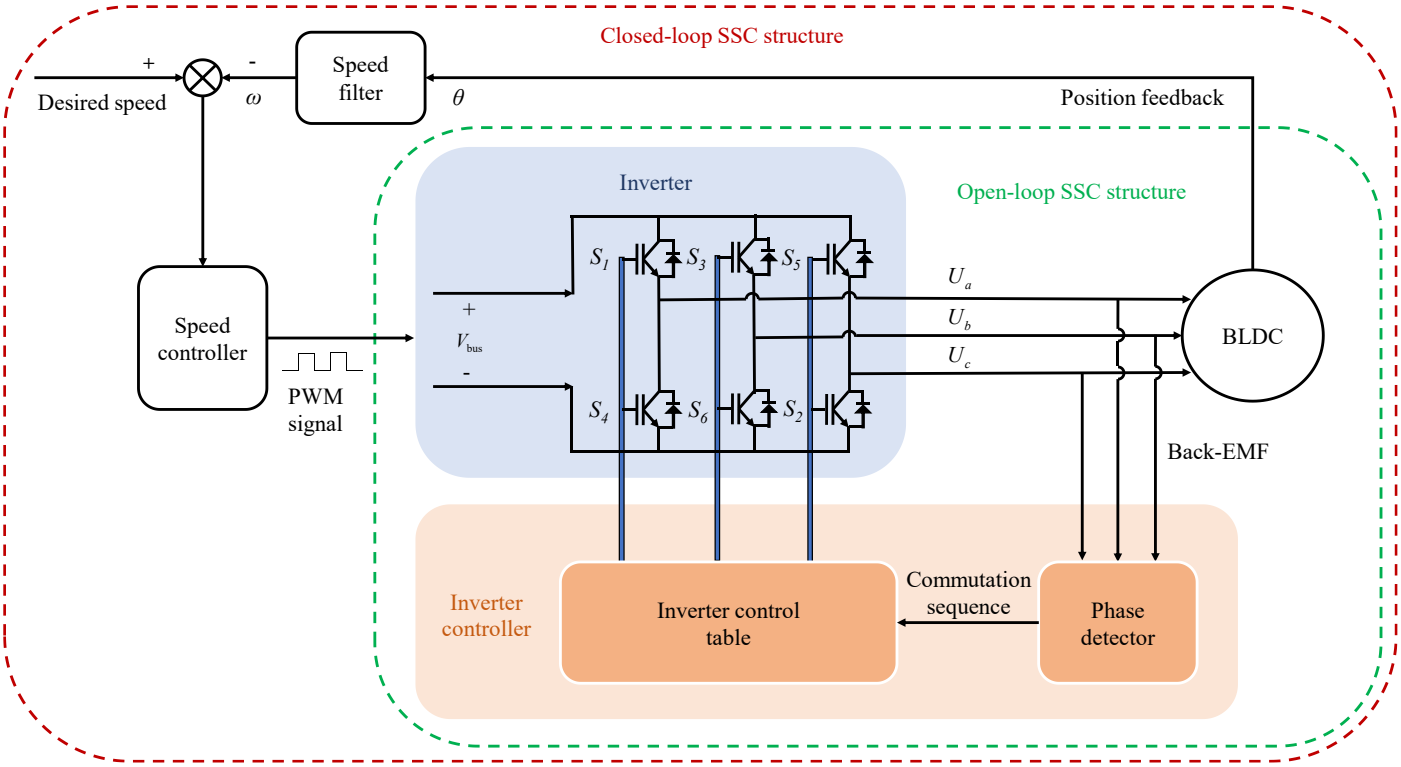

Fig. 1 Open-loop and closed-loop SSC structures

2.2 Closed-loop SSC structure

The thrust generated by the thruster is directly proportional to its rotational speed. A rotation sensor is essential to achieve precise thrust control. Commonly used rotation sensors include photoelectric, hall, and magnetic encoders. These sensors initially determine the exact position of the rotor and then use the differential method to calculate the speed. As shown in Fig. 1, the measured speed is then fed back to a PI controller that adjusts the output signal V_{bus} to form a closed-loop speed control system.

Compared with the open-loop SSC, the closed-loop SSC structure has the following advantages and disadvantages:

– The closed-loop SSC-driven thruster generates a more accurate thrust because a speed sensor and a PI controller are used.
– Similar to the open-loop SSC, six fixed magnetic field orientations result in high-frequency torque pulsation.
– The PI controller introduces additional inertia, which decreases the dynamic performance.

2.3 FOC structure

The FOC structure is similar to the closed-loop SSC. However, unlike the six fixed orientations in SSC, FOC can generate any magnetic field orientation. The key difference lies in how the three-phase voltages U_a, U_b, and U_c are generated. In SSC, these voltages are square waves owing to the characteristics of the inverters. In contrast, in FOC, high-frequency square waves (10–30 kHz) generated by SVPWM can be approximated as a continuous saddle-shaped wave. Additionally, a current controller is employed to achieve precise current control. Fig. 2 illustrates the FOC structure, where the Park transformation represents the coordinate transformation between the α-β stator coordinate and the d-q rotor coordinate, and the anti-

Park transformation is the inverse transformation. Taking the current transformation as an example, the Park transformation can be expressed as follows:

$$\begin{bmatrix} I_d \\ I_q \end{bmatrix} = \begin{bmatrix} \cos(\theta) & \sin(\theta) \\ -\sin(\theta) & \cos(\theta) \end{bmatrix} \begin{bmatrix} I_\alpha \\ I_\beta \end{bmatrix} \tag{1}$$

where I_q and I_d are the currents in d - q axes, I_α and I_β are the currents in α - β axes, and θ is the electrical angle. The Clark transformation that converts three-phase current to α - β axes can be written as follows:

$$\begin{bmatrix} I_\alpha \\ I_\beta \end{bmatrix} = \begin{bmatrix} 1 & -\frac{1}{2} & -\frac{1}{2} \\ 0 & \frac{\sqrt{3}}{2} & -\frac{\sqrt{3}}{2} \end{bmatrix} \begin{bmatrix} I_a \\ I_b \\ I_c \end{bmatrix} \tag{2}$$

with $I_a + I_b + I_c = 0$.

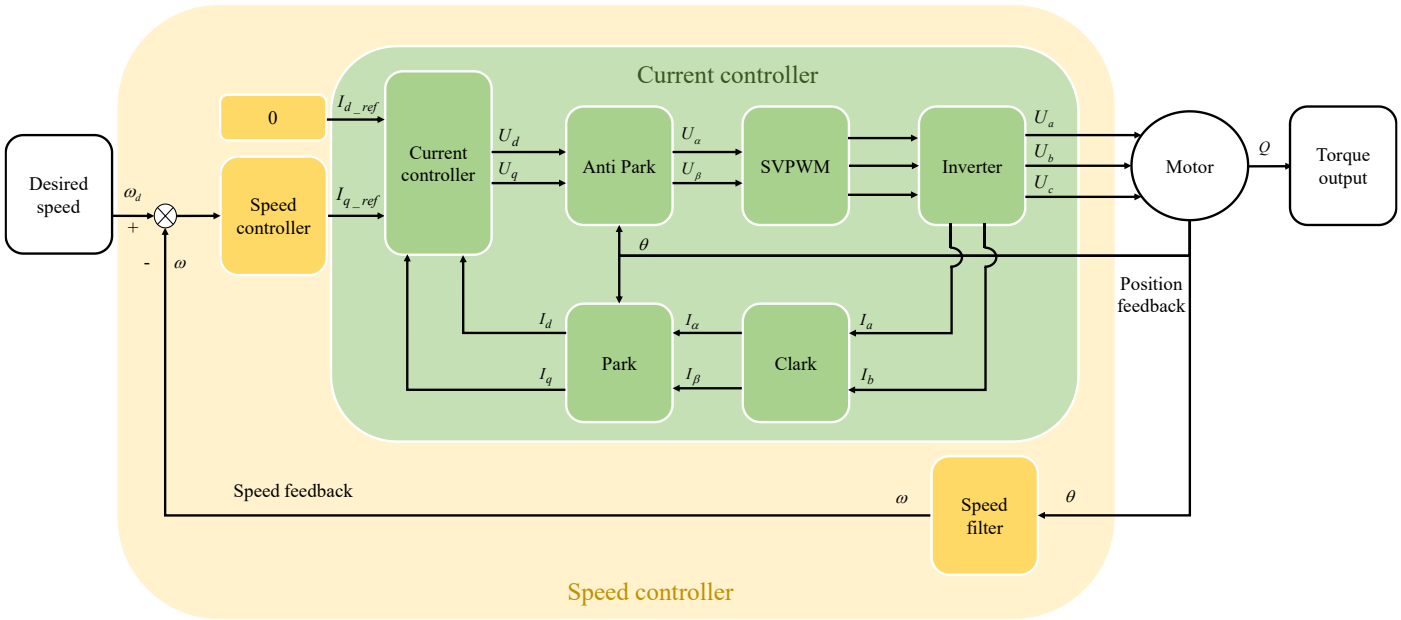

Fig. 2 FOC scheme diagram

In Fig. 3, the α - β axes represent the stator coordinate, and the d - q axes indicate the rotor coordinate. The voltages U_a, U_b and U_c are controlled by the inverter.

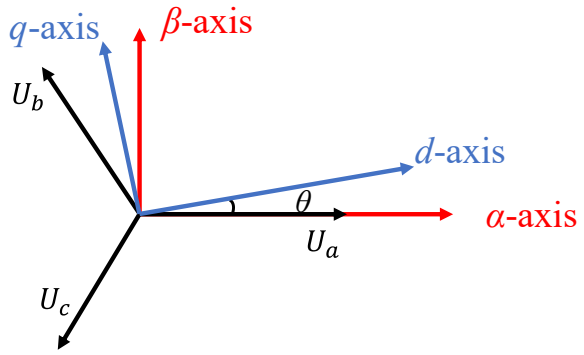

Fig. 3 Coordinate relationship diagram

The currents in d - q axes are directly related to the torque output Q by the motor, and Q can be expressed as follows:

$$Q = \frac{3p\left(\left(L_d - L_q\right)I_d + \psi\right)I_q}{2} \tag{3}$$

where L_q and L_d are the inductances in d - q axes, ψ is the flux linkage, and p is the number of pole pairs. A current controller is necessary as the relationship between voltage and current in d - q axes is complex, as shown below:

$$\begin{cases} U_d = R_s I_d + L_d \dot{I}_d - p\omega L_q I_q \\ U_q = R_s I_q + L_q \dot{I}_q - p\omega\left(L_d I_d + \psi\right) \end{cases} \tag{4}$$

where R_S is the phase resistance of the motor, and ω is the rotational speed. A PI controller is used for closed-loop current control.

Compared with open-loop and closed-loop SSC, the FOC structure offers several significant advantages:

- The closed-loop control of current and the continuous magnetic field orientation provide smooth torque transformation and torque pulsation reduction.
- As the field orientation is always aligned with the q -axis, the thruster driver delivers greater torque with lower energy consumption.

3. API structure

The API controller was compared with the conventional PI controller.

The conventional PI controller used in FOC speed closed-loop control offers the advantages of a simple structure and good performance, and it can be written as follows:

$$I_{q\_ref}(t) = K_p\omega_e(t) + K_i\int_0^t \omega_e(t)dt \tag{5}$$

where ω is rotational speed, ω_d is desired speed, $\omega_e = \omega_d - \omega$, $K_p = \chi_{\mathrm{PI}}K_{p0}$, and $K_i = \kappa_{\mathrm{PI}}K_{i0}$. χ_{PI}, κ_{PI}, K_{p0}, and K_{i0} are constants.

A novel API controller was proposed to enhance the performance of FOC-driven thrusters. As shown in Fig. 4, the adaptive laws were divided into two components: the adaptive proportional gain and the adaptive integral gain.

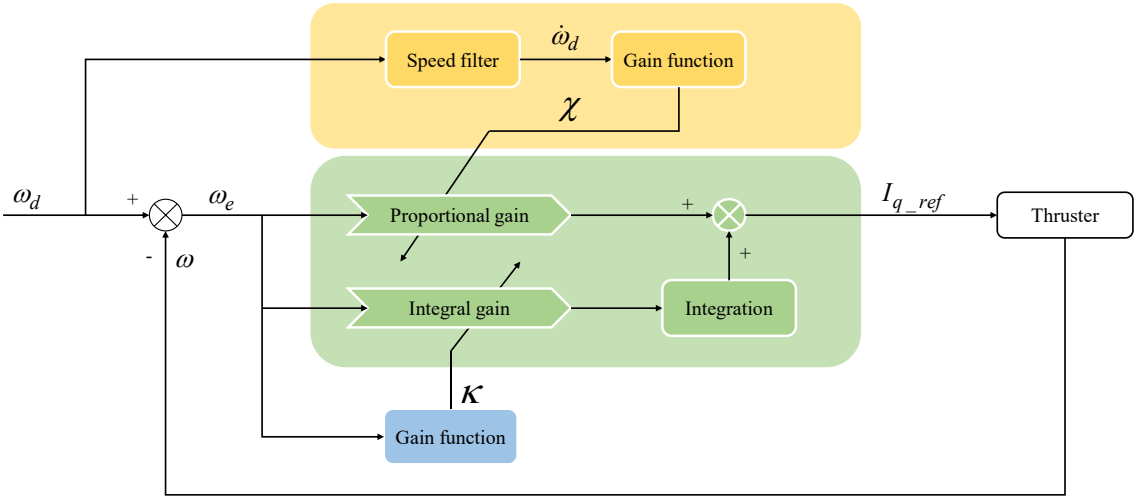

Fig. 4 API control scheme diagram

3.1 Adaptive proportional gain

The proportional gain in a conventional PI controller determines the error convergence speed and response speed to the input signal. A higher proportional gain results in faster convergence and response speed. Nevertheless, excessive gain can lead to overshoot and instability. An adaptive proportional gain law was proposed to achieve better performance than conventional PI controllers while avoiding overshoot and instability, which is expressed as follows:

$$K_{pa} = \chi K_{p0} \tag{6}$$

and

$$\chi = \mathrm{sat}\left(\left(\frac{\left|\dot{\omega}_d(t)\right|}{a} + \xi_p\right), \xi_p, \nu_p\right) \tag{7}$$

where K_{pa} is the adaptive proportional gain, and a, ξ_p, and ν_p are constants. sat(*,*lower*,*upper*) is a saturation function ensuring that the output value remains within the specified upper and lower limits. Eq. (7) outputs a low propositional gain to avoid instability at low speed and a high propositional gain to increase the response speed when the expected rotational speed changes dramatically.

In Eq. (7), $\dot{\omega}_d(t)$ represents the derivative of the expected rotational speed generated by a speed filter. The speed filter is defined as follows:

$$\begin{cases} \dot{z}_0(t) = k_1\left(\omega_d(t) - z_0(t)\right) + z_1(t) \\ \dot{z}_1(t) = k_2\left(\omega_d(t) - z_0(t)\right) \end{cases} \tag{8}$$

where $z_0(t)$ and $z_1(t)$ are the speed filter's output values. In Eq. (8), k_1 and k_2 are constants. The transfer functions with $\omega_d(t)$ as input and $z_0(t)$, $z_1(t)$ as outputs are as follows:

$$G_0(s) = \frac{Z_0(s)}{\Omega(s)} = \frac{k_1 s + k_2}{s^2 + k_1 s + k_2} \tag{9}$$

and

$$G_1(s) = \frac{Z_1(s)}{\Omega(s)} = \frac{k_2 s}{s^2 + k_1 s + 1} \tag{10}$$

where $Z_0(s)$, $Z_1(s)$, and $\Omega(s)$ are the Laplace transformations of $z_0(t)$, $z_1(t)$, and $\omega_d(t)$, respectively. The speed filter structure is the same as the second-order system in Section 8.2.6 of [30]. If the values of k_1 and k_2 are appropriate, $z_0(t)$ and $z_1(t)$ will converge to $\omega_d(t)$ and $\dot{\omega}_d(t)$, respectively.

In summary, the adaptive proportional gain is determined by the rate of change in rotational speed. In the case of a low rate, the gain is reduced to prevent overshoot and instability. Conversely, when the rate of change is high, the gain is increased to improve the response speed.

3.2 Adaptive integral gain

A constant integral gain results in varying step responses to different step signals. While a large amplitude can lead to overshoot, a small amplitude can result in undershoot. An improved adaptive integral gain law was proposed to address this issue. This law can be expressed as follows:

$$K_{ia} = \kappa K_{i0} \tag{11}$$

and

$$\kappa = \mathrm{sat}\left(\left(\nu_i - \frac{|\omega_e(t)|}{b}\right), \xi_i, \nu_i\right) \tag{12}$$

where K_{ia} is the adaptive integral gain, and b, ξ_i, and ν_i are constants. When the rotational speed error is high, Eq. (12) outputs a low integral gain to limit the integral term and avoid potential overshoot and a high integral gain to increase the convergence speed when the speed error is small.

Similar to the ISPI control strategy, the adaptive integral gain law ensures a small gain when the error is large and a large gain when the error is small. This approach effectively prevents overshoot and undershoot across different step signal amplitudes.

4. Simulations

A series of simulations was conducted in MATLAB/Simulink to highlight the advantages of the API controller for underwater thrusters, which encompassed both frequency sweep and step signal response. For the conventional PI speed controller with FOC, various PI gain settings were evaluated in the simulation. For the API controller, given that the typical rotational speed of the thruster ranges from 5,00 to 2,000 rpm, the load torque in the thruster can be expressed as $Q_L = \left(\pi\omega(t)/30\right)^2 / 256000$. The adaptive parameters are listed in Table 2.

Table 2 Adaptive parameters

Parameters	a	ξ_p	ν_p	b	ξ_i	ν_i	K_{p0}	K_{i0}
Values	200	8	40	200	0	6	1.5×10^{-3}	6.1×10^{-3}

4.1 Adaptive integral terminal sliding mode controller

This subsection presents the AITSMC for speed control. The dynamics model of the thruster is as follows:

$$J\dot{\omega} = f(\omega) + Q + \Delta \tag{13}$$

where J is the rotational inertia of the shaft, $f(\omega)$ is the friction, Q is the output torque, and friction $f(\omega)$ is assumed to be known. Δ is the external torque load, and it can be observed using a finite-time observer:

$$\begin{cases} \dot{\tilde{\omega}} = -600\left|\tilde{\omega} - \omega\right|^{1/2} \mathrm{sign}(\tilde{\omega} - \omega) + f(\omega)/J + Q/J + \tilde{\Delta}/J \\ \dot{\tilde{\Delta}} = -100\,\mathrm{sign}(\tilde{\omega} - \omega) \end{cases} \tag{14}$$

where $\tilde{\Delta}(0) = 0$ and $\tilde{\omega}(0) = 0$. Within a finite time, $\tilde{\Delta}$ will converge to Δ.

The AITSMC structure can be written as follows:

$$\begin{cases} s_\omega = \omega_e + \alpha_{\mathrm{AITSMC}}\omega_{I,e} \\ \dot{\omega}_{I,e} = \mathrm{sign}(\omega_e)\left|\omega_e\right|^{1/3} \end{cases} \tag{15}$$

where s_ω is the sliding surface, $\omega_{I,e}(0) = -\omega(0)/\alpha_{\mathrm{AITSMC}}$, and α_{AITSMC} is a constant parameter.

Then, the derivative of the sliding surface is as follows:

$$\dot{s}_\omega = \dot{\omega}_d - (f(\omega) + Q + \tilde{\Delta})/J + \alpha_{\mathrm{AITSMC}}\dot{\omega}_{I,e} \tag{16}$$

If the sliding surface converges to zero, the output torque should be as follows:

$$Q = J\left(-f(\omega)/J - \tilde{\Delta}/J + \dot{\omega}_d + \alpha_{\mathrm{AITSMC}}\dot{\omega}_{I,e} + K_1\left|s_\omega\right|^{1/2}\mathrm{sign}(s_\omega) + K_2 s_\omega\right) \tag{17}$$

where K_2 is a constant parameter, and K_1 is an adaptive parameter. K_1 can be calculated as follows:

$$\dot{K}_1 = \begin{cases} k\mathrm{sign}(\left|s_\omega\right| - \mu), K_1 > K_{\min} \\ K_{\min}, K_1 \le K_{\min} \end{cases} \tag{18}$$

where k, μ, and $K_{\min}$ are constant parameters. Then, I_{d_ref} is set to zero, and I_{q_ref} can be driven by Eqs. (3) and (17).

4.2 Frequency sweep simulations

The thruster must generate a time-varying thrust under the influence of an external disturbance to maintain stable sailing, for which the thruster output dynamics must be considered. A series of closed-loop amplitude and phase response tests were performed to compare the dynamic performances of PI and API controllers and AITSMC in FOC-driven thrusters. The desired motor rotational speed can be expressed as $\omega_d = 700\sin(\Omega t) + 800$ with $\Omega = 0.1\times 1.3^{(t/5)}$. The desired signal frequency increases with time. Subsequently, their responses were analyzed in the frequency domain.

As depicted in Fig. 5, the amplitude is equal to $20\log\left(\left|\mathcal{F}\right|(\omega(t))/\left|\mathcal{F}\right|(\omega_d(t))\right)$, and the phase is equal to $180\left(\angle\mathcal{F}(\omega(t)) - \angle\mathcal{F}(\omega_d(t))\right)/\pi$. The amplitude should be zero when the rotational speed error converges, and it decreases as the frequency increases. The frequency corresponding to an amplitude of −3 dB is defined as the amplitude bandwidth. A higher bandwidth indicates better dynamics performance, similar to the phase bandwidth. For the PI controller, $K_p = 13K_{p0}$ and $K_i = 6K_{i0}$. For the AITSMC, $\alpha_{\mathrm{AITSMC}} = 900$ and $K_2 = 70$. As shown in Fig. 6, the proportional gain increases with frequency, resulting in a higher amplitude bandwidth.

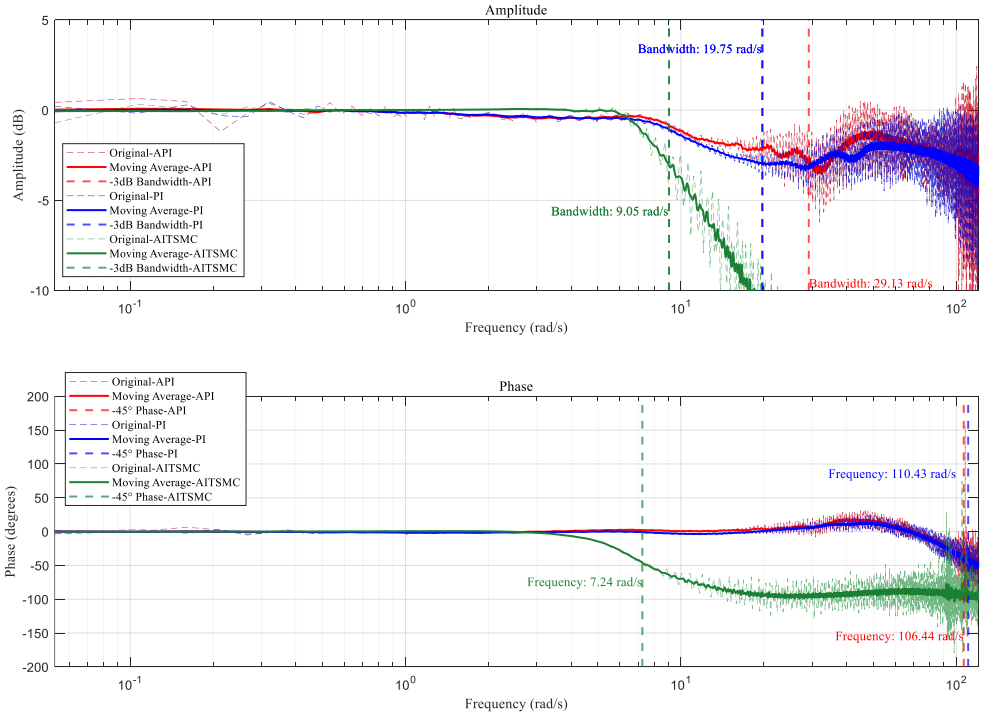

Fig. 5 Closed-loop responses in the frequency domain for FOC

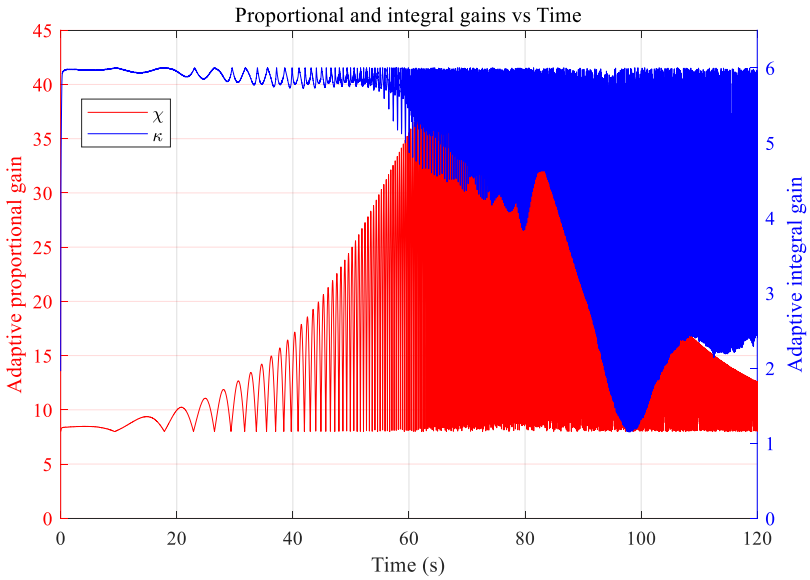

Fig. 6 API adaptive control parameters in the time domain

Although a higher proportional gain leads to a greater amplitude bandwidth, it also increases instability. In Fig. 7, the red line shows the PI control response when $K_p = 13K_{p0}$, and the blue line represents $K_p = 15K_{p0}$. Therefore, the amplitude bandwidth in a conventional PI controller is limited by instability. The API controller overcomes this limitation by adapting the proportional gain.

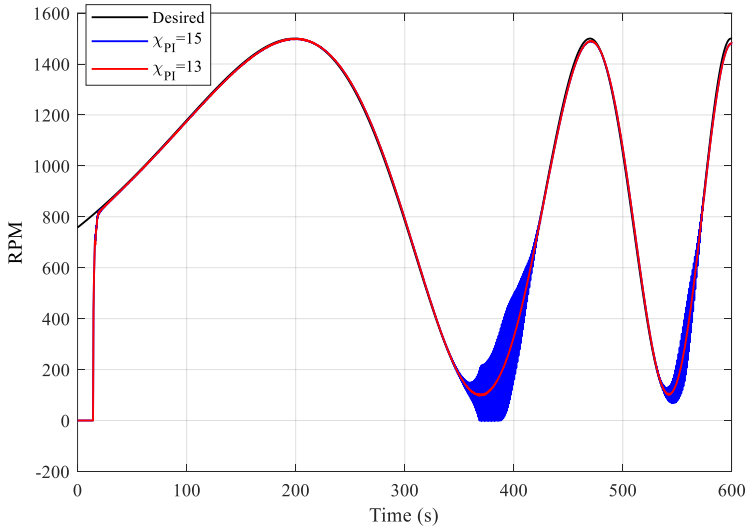

Fig. 7 PI control cases with different parameters

As shown in Fig. 8, the speed filter generates a smooth time-varying $\dot{\omega}_d(t)$, preventing divergence even at extremely high frequencies.

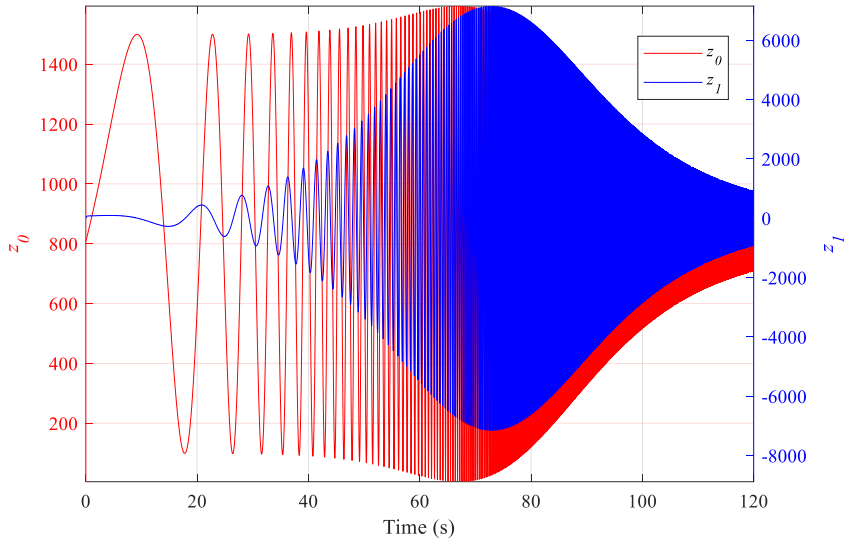

Fig. 8 Speed filter outputs in API controller

The closed-loop responses are depicted in Fig. 9. The open-loop SSC structure achieves a significantly higher amplitude bandwidth. In contrast, the closed-loop SSC structure trades off dynamic response performance for precise rotational speed control.

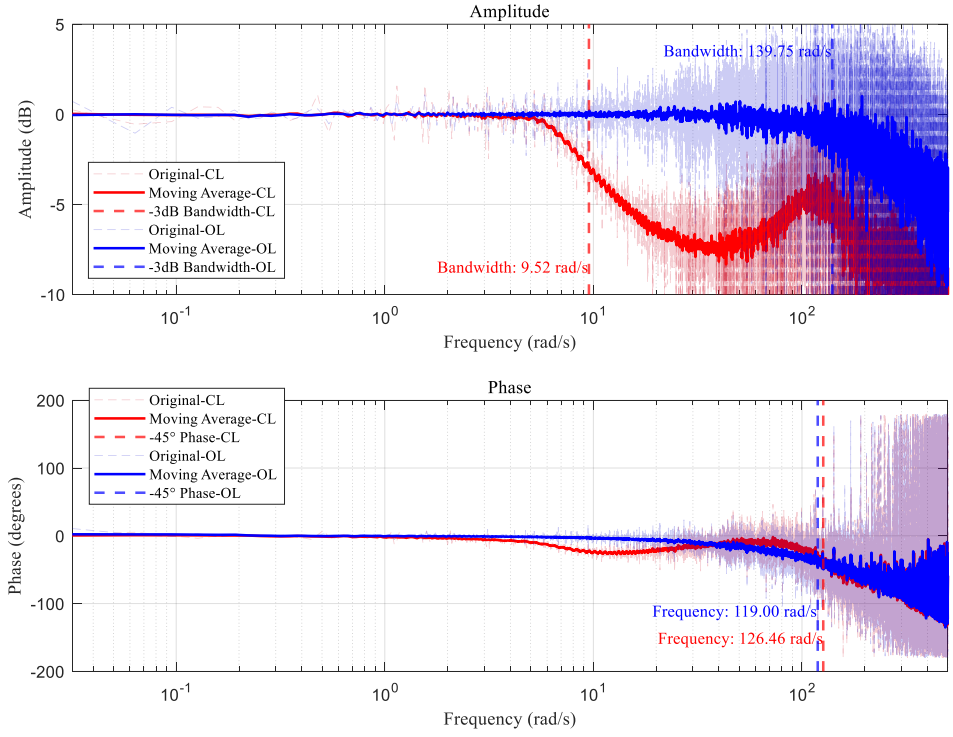

Fig. 9 Closed-loop responses in the frequency domain for open-loop (OL) SSC and closed-loop (CL) SSC

4.3 Step signal simulations

A conventional PI controller exhibits varying performances in response to step signals of different amplitudes. As shown in Fig. 10, $K_p = 8K_{p0}$ and $K_i = 6K_{i0}$ in the PI controller and $\alpha_{\text{AITSMC}} = 900$ and $K_2 = 70$ in the AITSMC. While the PI controller performs well for a 1,000 rpm step signal, it displays overshoot when the step signal increases to 1,500 rpm. The response characteristics of AITSMC under various

signals are consistent, but the rise time is longer and overshoot is always observed. The strategy of ISPI is commonly employed to address this issue, where the integral gain is given as follows:

$$\beta = \begin{cases} 10, |\omega_e(t)| < 500 \\ 0, |\omega_e(t)| \geq 500 \end{cases} \tag{19}$$

However, the thruster load torque in water depends on the rotational speed. High-amplitude step signals decrease the convergence rate because of the considerable load during integration. The adaptive integral gain law stated in Eq. (7) shows superior performance in underwater thrusters.

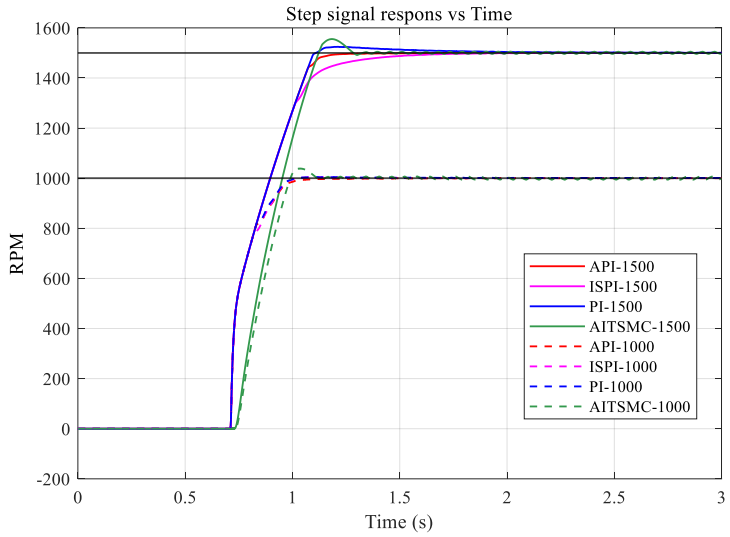

Fig. 10 Step signal responses for FOC

Compared with SSC-driven thrusters, as shown in Fig. 11, open-loop SSC-driven thrusters achieve an ultrafast response time. Nonetheless, the direct conversion of the rotational speed command to the voltage command introduces an inevitable static state error. In addition, as the SSC structure does not control the current, high-frequency chattering occurs in all SSC-driven thrusters.

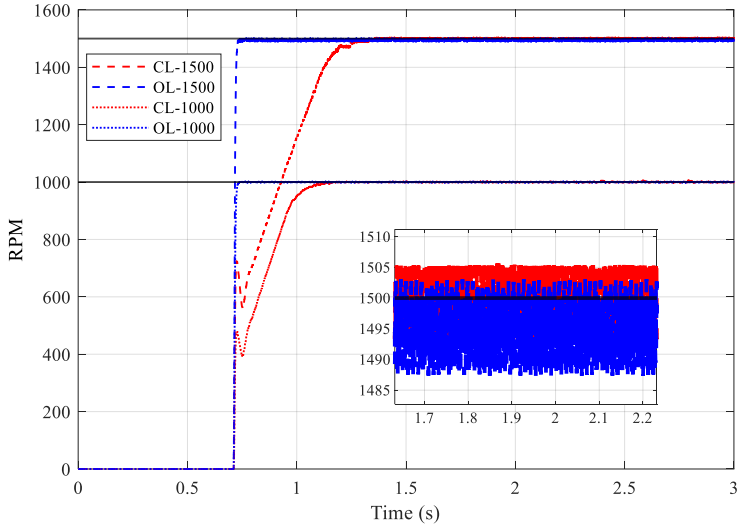

Fig. 11 Step signal responses for open-loop (OL) SSC and closed-loop (CL) SSC

In Fig. 12, the red and blue lines represent the mechanical and electrical powers of the SSC- and FOC-driven thrusters, respectively. The mechanical power can be written as $P_m = \omega Q_L$, and the electrical power as

$P_e = U_a I_a + U_b I_b + U_c I_c$. On average, the mechanical and electrical powers of the SSC are 7.7639 W and 13.5442 W, respectively, resulting in an energy efficiency of 57.3%. In contrast, the energy consumption of the FOC-driven thruster is more stable, with average mechanical and electrical powers of 7.7628 W and 9.6847 W, respectively, achieving an energy efficiency of up to 80.2%.

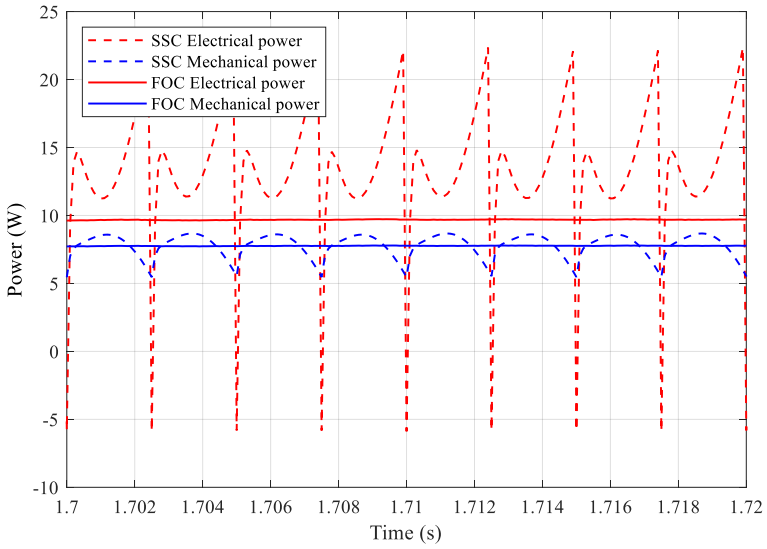

Fig. 12 Mechanical and electrical powers at 1,000 rpm

4.4 Thruster output simulations

The performance of rotational speed controllers should be analyzed in a realistic underwater environment to the best possible extent. Therefore, the thrust output sequence in [28] was used as the desired rotational speed signal.

Figure 13 shows that the output thrust is considered as $T = \omega^3 / (200|\omega|)$. The API and PI controllers and AITSMC meet the thrust controller's dynamic performance requirements. The average steady-state errors between 10 s and 50 s are 1.0768 rpm, 1.1933 rpm, and 4.8336 rpm for the API and PI controllers and AITSMC, respectively. Moreover, between 70 s and 100 s, the corresponding errors are 1.1201 rpm, 1.2379 rpm, and 4.9738 rpm, respectively.

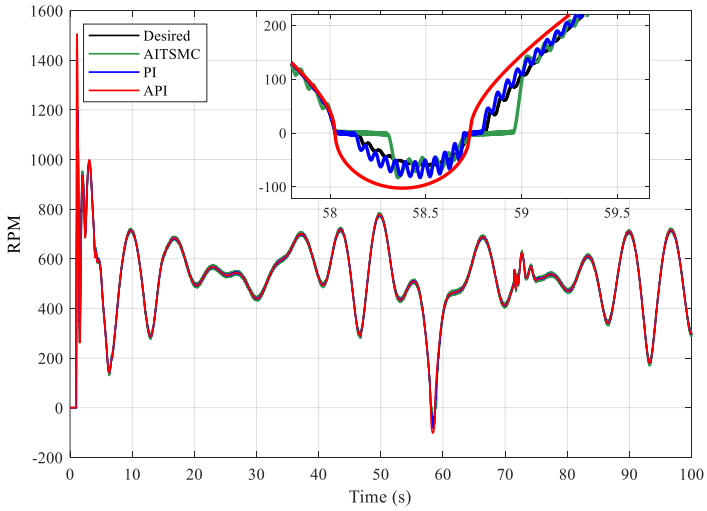

Fig. 13 Realistic signal responses

Notably, at 68.5 s, the desired speed is less than zero, and the static friction and "cogging effect" of the motor are much greater than the water resistance. Owing to the higher proportional gain of the PI controller at 68.5 s, significant chattering occurs in the PI controller at low speed. Considering the steady-state error and the chattering at low speed, the API controller demonstrates superior performance for underwater thrusters.

4.5 Parametric analysis

As comparison controllers, the PI controller and AITSMC should be well-tuned. Tables 3 and 4, comprising a series of parameters and their corresponding performance indicators, serve as the basis for parameter selection.

As depicted in Table 3, the effect of the parameters on the performance can be summarized as follows: 1) The larger the χ_{PI} and κ_{PI}, the higher the amplitude bandwidth. The impact of χ_{PI} on the amplitude bandwidth is much greater than that of κ_{PI}; 2) The larger the χ_{PI} and κ_{PI}, the smaller the rise time. However, an excessively high κ_{PI} will cause higher overshoot and larger settling time; 3) The electric current will limit the rise time, and an excessively high χ_{PI} will lead to instability at low speed, as shown in Fig. 7.

Considering all aspects of performance comprehensively, in frequency sweep simulations, $\chi_{\mathrm{PI}}=13$ and $\kappa_{\mathrm{PI}}=6$. In step signal simulations, the desired signal is a constant value; thus, $\chi_{\mathrm{PI}}=\chi=8$.

Furthermore, the parameter selection for the API controller is based on Table 3, and the upper limit of κ is set to 6 to avoid overshoot. The lower limit of χ is set to 8 to avoid instability at low speed, and the upper limit is set to 40 to increase the amplitude bandwidth.

Table 3 PI controller performance at 1,000 rpm step signal

χ_{PI}	κ_{PI}	**Rise time**	**Overshoot**	**Settling time**	**Amplitude bandwidth**	**Frequency bandwidth**
8	4	0.1928 s	0.08 %	0.3365 s	15.02 rad/s	111.50 rad/s
8	6	0.1808 s	0.48 %	0.2543 s	15.60 rad/s	111.50 rad/s
8	8	0.1754 s	1.25 %	0.2426 s	15.71 rad/s	111.50 rad/s
13	4	0.1455 s	0.01 %	0.3738 s	19.12 rad/s	111.43 rad/s
13	6	0.1455 s	0.16 %	0.2436 s	19.75 rad/s	110.43 rad/s
13	8	0.1455 s	0.59 %	0.2408 s	20.98 rad/s	110.43 rad/s
15	6	0.1455 s	0.22 %	0.2821 s	20.93 rad/s	109.32 rad/s

For AITSMC, after extensive testing, α_{AITSMC} and K_2 are the key parameters that affect performance. As shown in Table 4, considering all aspects of performance comprehensively, α_{AITSMC} is set to 900 and K_2 to 70 in the frequency sweep and step signal simulations.

Table 4 AITSMC performance at 1,000 rpm step signal

α_{AITSMC}	K_2	**Rise time**	**Overshoot**	**Settling time**	**Amplitude bandwidth**	**Frequency bandwidth**
500	70	0.3246 s	1.38 %	0.3916 s	5.38 rad/s	4.79 rad/s
700	70	0.2354 s	2.28 %	0.3722 s	7.61 rad/s	6.12 rad/s
900	70	0.1934 s	3.84 %	0.3394 s	9.05 rad/s	7.24 rad/s
900	50	0.2162 s	2.67 %	0.3653 s	7.88 rad/s	6.28 rad/s
900	90	0.1839 s	5.42 %	0.3274 s	9.90 rad/s	7.77 rad/s
1200	70	0.1699 s	8.25 %	0.3766 s	10.60 rad/s	7.77 rad/s

5. Experiments

A series of experiments using the step signal was conducted on an existing platform to analyze and compare the performances of FOC- and SSC-driven underwater thrusters. The thrusters' rotation speed, torque, and average input current were measured to evaluate the stability, thrust control accuracy, and energy consumption, respectively.

5.1 Experimental platform

As shown in Fig. 14, all the components were arranged vertically to minimize the effect of gravity. The propeller was connected to the motor's rotor via a coupling, whereas the motor's stator was fixed to the encoder. The torque was then transmitted to the torque sensor. The key parameters of the experimental platform are presented in Table 5.

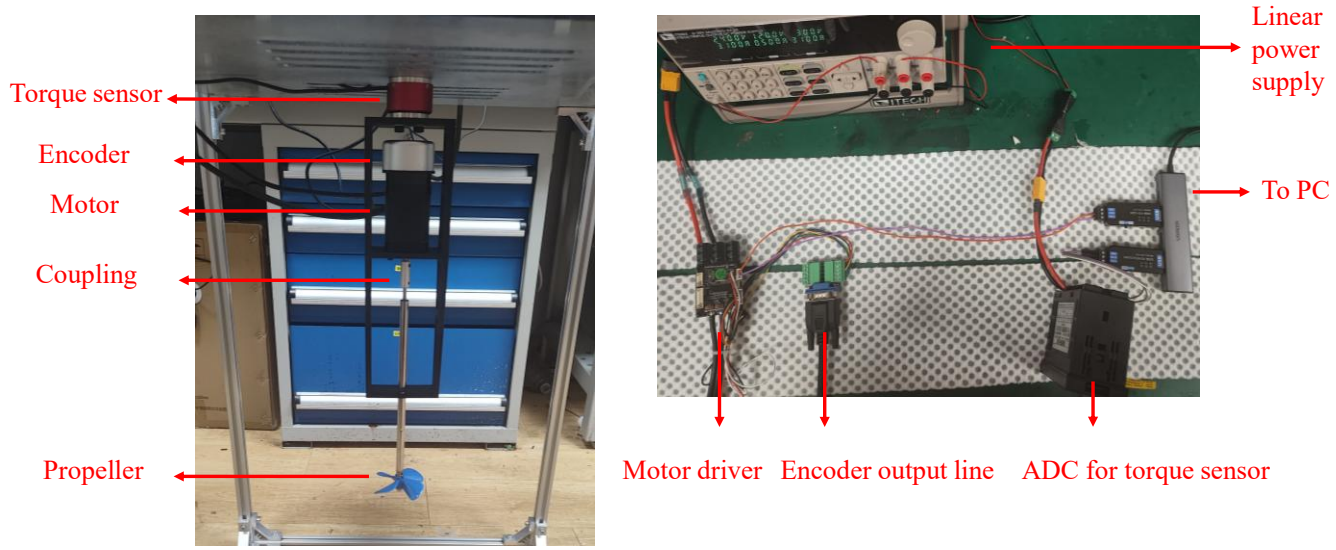

Fig. 14 Experimental platform

Table 5 Experimental platform parameters

Items	Value	Unit
Motor pole pairs	4	-
KV rating	250	rpm/V
Motor phase resistance	0.89	Ω
Motor phase inductance	620	μH
Motor bus voltage	24	V
Count per revolution of the encoder	4000	-
Propeller diameter	70	mm
Range of the torque sensor	0–1	N·m
Sensitivity of the torque sensor	1.34	mV/V

5.2 Experimental results

The simulation results showed that the bandwidths of the PI and API controllers were much greater than those of AITSMC. Moreover, the API controller was better than PI in terms of amplitude bandwidth. Subsequently, a comparison experiment between PI and API controllers was performed to confirm the tentative conclusions of the simulation. The adaptive parameters of the API were the same as those in

Table 2, except for the following differences: $K_{p0}=6\times10^{-4}$ and $K_{i0}=8\times10^{-3}$. For the PI controller, K_{p0} and K_{i0} were the same as those of the API controller: $\chi_{\mathrm{PI}}=8$ and $\kappa_{\mathrm{PI}}=4.5$. Fig. 15 shows that both the amplitude and phase bandwidths of the API controller were greater than those of the PI controller. In Fig. 16, the PI controller achieved the shortest rise time, and the rise time of the API controller was longer while the overshoot was avoided. In Fig. 17, the SSC-driven thruster exhibited a low torque output in the absence of an electric current control, leading to a much longer rise time in Fig. 16. Table 6 shows the average input current for the motor. The energy consumption of the FOC was 18.75% lower than that of the SSC at 600 rpm and 15.09% lower than that of the SSC at 1,200 rpm.

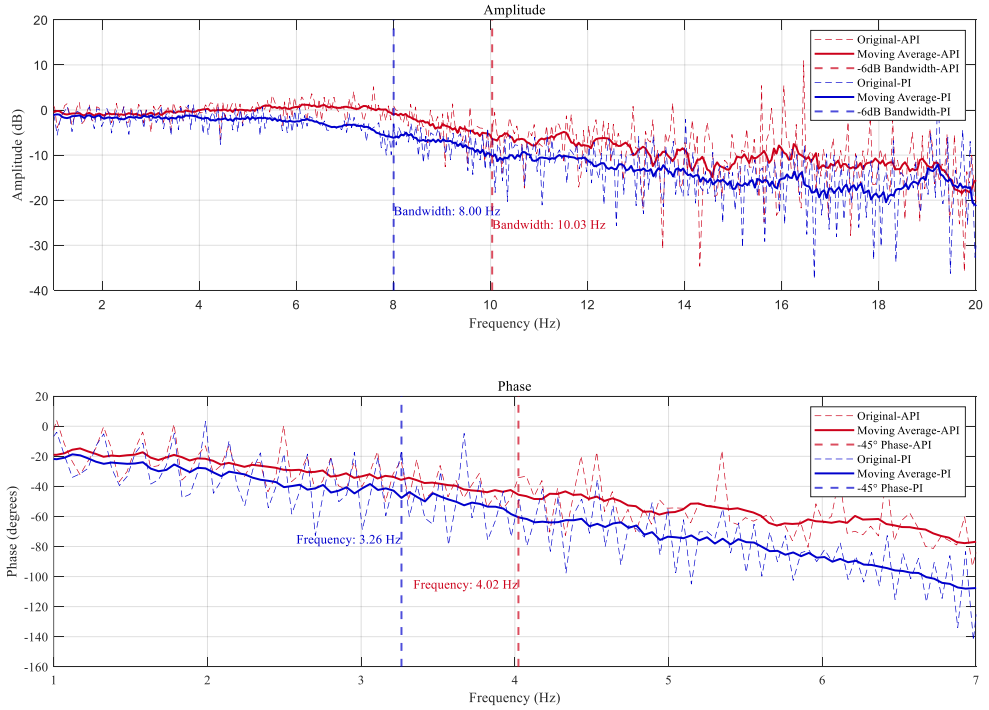

Fig. 15 Experimental responses in the frequency domain for FOC

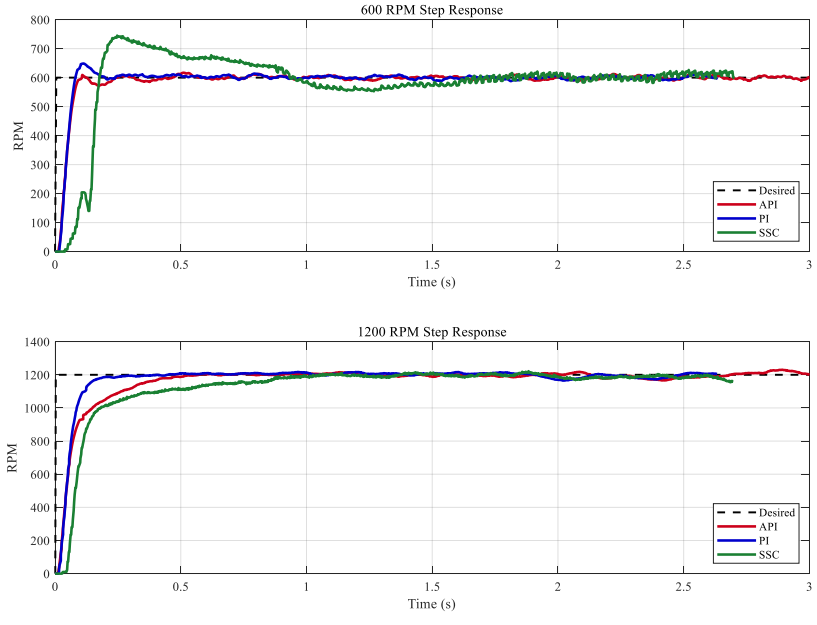

Fig. 16 Experimental speed responses for the step signal

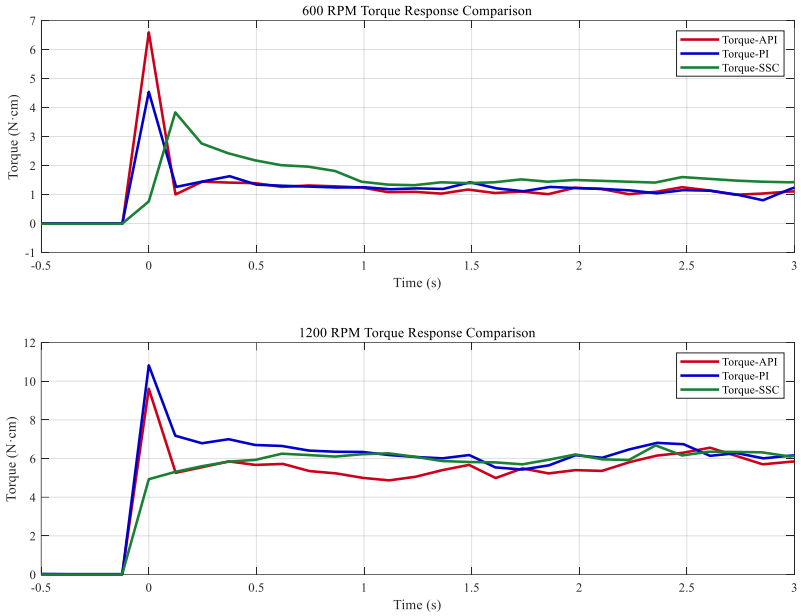

Fig. 17 Experimental torque responses for the step signal

Table 6 Average input currents (read from the linear power supply)

Cases	Average input currents (mA)
PI-SSC at 600 rpm	160
PI-SSC at 1,200 rpm	530
PI-FOC at 600 rpm	130
PI-FOC at 1,200 rpm	450
API-FOC at 600 rpm	130
API-FOC at 1,200 rpm	450

6. Conclusion

This paper comparatively evaluated open-loop SSC, closed-loop SSC, and FOC for underwater thrusters by introducing a novel API speed controller. The simulations established that the dynamic performance of open-loop SSC-driven systems was excellent, with the −3 dB bandwidth reaching 139.75 rad/s. This outstanding advantage is responsible for the extensive use of open-loop SSC controllers despite their lack of precision. Conversely, the closed-loop controller achieved high accuracy but exhibited a reduced bandwidth of 9.52 rad/s. The FOC ensured precise speed control with lower energy consumption and avoided the high-frequency speed chattering in SSC. Additionally, the conventional PI speed controller for FOC-driven thrusters struck a balance in bandwidth, achieving a response frequency of 19.75 rad/s at −3 dB magnitude. However, this conventional PI controller had limitations under a torque load in water. The proposed API speed controller displayed superior dynamic response and reduced chattering at low speeds compared with conventional PI controllers, with a −3 dB bandwidth of 29.13 rad/s. Its step responses in water were consistent and outperformed those of both PI and ISPI controllers. The experiments supported the partial conclusions of the simulation, including the higher bandwidth of the API controller, API overshoot avoidance, energy saving, and higher torque output of the FOC-driven motor. Given these advantages, the API FOC-driven thruster is poised to play a crucial role in future docking [31], hovering [32], and other marine missions [33].

7. Acknowledgments

The authors acknowledge the support from the National Key R&D Program of China (Grant No. 2023YFC2812800) and the National Natural Science Foundation of China (Grant No. 42376187).

REFERENCES

[1] Mukherjee, K., Kar, I. N., Bhatt, R. K. P., 2015. Region tracking based control of an autonomous underwater vehicle with input delay. *Ocean Engineering*, 99, 107-114. https://doi.org/10.1126/scirobotics.abe1901

[2] Hou, Y., Wang, H., Wei, Y., Iu, H. H. C., Fernando, T., 2023. Robust adaptive finite-time tracking control for intervention-AUV with input saturation and output constraints using high-order control barrier function. *Ocean Engineering*, 268, 113219. https://doi.org/10.1016/j.oceaneng.2022.113219

[3] Yu, C., Zhong, Y., Lian, L., Xiang, X., 2023. Adaptive simplified surge-heading tracking control for underwater vehicles with thruster's dead-zone compensation. *Nonlinear Dynamics*, 111(14), 13073-13088. https://doi.org/10.1007/s11071-023-08512-9

[4] Kiss-Nagy, K., Simongáti, G., 2025. Digital twin of USV thruster based on CFD simulations and towing tank experiments. *Brodogradnja*, 76(4), 1-17. https://doi.org/10.21278/brod76403

[5] Guzelbulut, C., Badalotti, T., Suzuki, K., 2025. Impact of control strategies for wind-assisted ships on energy consumption. *Brodogradnja*, 76(1), 1-14. https://doi.org/10.21278/brod76104

[6] Wang, Z., Wei, Z., Yu, C., Cao, J., Yao, B., Lian, L., 2023. *Dynamic modeling and optimal control of a positive buoyancy diving autonomous vehicle. Brodogradnja*, 74(1), 19-40. https://doi.org/10.21278/brod74102

[7] Xu, J., Wei, S., Yin, L., 2024. Communication topology for AUV formation consensus based on optimal cost control under time-varying communication and input delays. *Ocean Engineering*, 304, 117906. https://doi.org/10.1016/j.oceaneng.2024.117906

[8] Yan, H., Xiao, Y., Zhang, H., 2023. Practical fixed-time adaptive NN fault-tolerant control for underactuated AUVs with input quantization and unknown dead zone. *IEEE Access*, 11, 118973-118982. https://doi.org/10.1109/ACCESS.2023.3326442

[9] Deutsch, C., Moratelli, L., Thuné, S., Kuttenkeuler, J., Söderling, F., 2018. Design of an AUV research platform for demonstration of novel technologies. *Proceedings of 2018 IEEE/OES Autonomous Underwater Vehicle Workshop*, 1-8. https://doi.org/10.1109/AUV.2018.8729729

[10] Ljulj, A., Slapničar, V., Brigić, J., 2022. Unmanned surface vehicle - Tritor. *Brodogradnja*, 73(3), 135-150. https://doi.org/10.21278/brod73308

[11] Singh, S., Gorla, N. B. Y., Jayaraman, K., Pou, J., 2022. Analysis and mitigation of the common-mode noise in a three-phase SiC-based brushless DC motor drive with 120° conduction mode. *IEEE Transactions on Power Electronics*, 37(5), 5514-5523. https://doi.org/10.1109/TPEL.2021.3133880

[12] Yang, L., Xiang, X., Kong, D., Yang, S., 2024. Small modular AUV based on 3D printing technology: design, implementation and experimental validation. *Brodogradnja*, 75(1), 1-16. https://doi.org/10.21278/brod75104

[13] Patel, H. V., 2022. Modified sinusoidal pulse width modulation technique for speed control of permanent magnet brushless DC motor (Thesis). Maharaja Sayajirao University of Baroda.

[14] Healey, A.J., Rock, S.M., Cody, S., Miles, D., Brown, J.P., 1995. Toward an improved understanding of thruster dynamics for underwater vehicles. *IEEE Journal of Oceanic Engineering*, 20(4), 354-361. https://doi.org/10.1109/48.468252

[15] Kim, J., Chung, W.K., 2006. Accurate and practical thruster modeling for underwater vehicles. *Ocean Engineering*, 33(5), 566-586. https://doi.org/10.1016/j.oceaneng.2005.07.008

[16] Kanevskii, G., Klubnichkin, A., Sazonov, K., 2020. Propulsion performance prediction method for multi shaft vessels. *Brodogradnja*, 71(3), 27-36. https://doi.org/10.21278/brod71303

[17] Aras, M.S.M., Abdullah, S.S., Rahman, A.Ab., Aziz, M.A.A., 2013. Thruster modelling for underwater vehicle using system identification method. *International Journal of Advanced Robotic Systems*, 10(5), 252. https://doi.org/10.5772/56432

[18] Sharma, P. K., Sindekar, A. S., 2016. Performance analysis and comparison of BLDC motor drive using PI and FOC. *Proceedings of 2016 International Conference on Global Trends in Signal Processing, Information Computing and Communication*, 485-492. https://doi.org/10.1109/ICGTSPICC.2016.7955350

[19] Davis, C.J., 2023. Acoustic Minimization of Ocean Twilight Zone Vehicle, Mesobot (Thesis). Massachusetts Institute of Technology.

[20] Widy, A., Woo, K.T., 2017. Robust attitude estimation method for underwater vehicles with external and internal magnetic noise rejection using Adaptive Indirect Kalman Filter. *Proceedings of 2017 IEEE/RSJ International Conference on Intelligent Robots and Systems (IROS)*, 2595-2600. https://doi.org/10.1109/IROS.2017.8206082

[21] Jiang, S., Zhang, B., Shuai, C., Yu, S., 2023. Comparison of different control strategies for brushless direct current (BLDC) motors on AUVs. *Proceedings of the 33rd International Ocean and Polar Engineering Conference*, 1872-1878.

[22] Kim, S., Yoon, Y.-D., Sul, S.-K., Ide, K., 2013. Maximum torque per ampere (MTPA) control of an IPM machine based on signal injection considering inductance saturation. *IEEE Transactions on Power Electronics*, 28(1), 488-497. https://doi.org/10.1109/TPEL.2012.2195203

[23] Simanek, J., Novak, J., Cerny, O., Dolecek, R., 2008. FOC and flux weakening for traction drive with permanent magnet synchronous motor. *Proceedings of 2008 IEEE International Symposium on Industrial Electronics*, 753-758. https://doi.org/10.1109/ISIE.2008.4677099

[24] Paolucci, L., Grasso, E., Grasso, F., König, N., Pagliai, M., Ridolfi, A., Rindi, A., Allotta, B., 2019. Development and testing of an efficient and cost-effective underwater propulsion system. *Proceedings of Institution of Mechanical Engineers*, 1309-1328. https://doi.org/10.1177/0959651819829627

[25] Zhao, S., 2024. FOC motor control system and simulation based on fuzzy PID control. *Proceedings of 2023 International Conference on Mechatronic Automation and Electrical Engineering*, 040016. https://doi.org/10.1063/5.0214190

[26] Nicola, M., Nicola, C.-I., DUȚĂ, M., 2020. Sensorless control of PMSM using FOC Strategy based on LADRC speed controller. *Proceedings of the 12th International Conference on Electronics, Computers and Artificial Intelligence (ECAI)*. 1-6. https://doi.org/10.1109/ECAI50035.2020.9223129

[27] Blanke, M., Lindegaard, K.-P., Fossen, T.I., 2000. Dynamic model for thrust generation of marine propellers. *Proceedings of the 5th IFAC Conference on Manoeuvring and Control of Marine Craft (MCMC)*, 353–358. https://doi.org/10.1016/S1474-6670(17)37100-8

[28] Shen, K., Yu, C., Guo, Y., Zhong, Y., Cao, J., Xiang, X., Lian, L., 2024. Hybrid-tracked finite-time path following control of underactuated underwater vehicles with 6-DOF. *Ocean Engineering*, 312, 119023. https://doi.org/10.1016/j.oceaneng.2024.119023

[29] Gonzalez-Garcia, A., Castañeda, H., 2021. Adaptive integral terminal sliding mode control for an unmanned surface vehicle against external disturbances. *Proceedings of the 13th IFAC Conference on Control Applications in Marine Systems, Robotics, and Vehicles (CAMS)*. 202–207. https://doi.org/10.1016/j.ifacol.2021.10.094

[30] Fossen, T.I., 2011. Handbook of marine craft hydrodynamics and motion control. John Wiley & Sons, Ltd, Hoboken, New Jersey, USA. https://doi.org/10.1002/9781119994138

[31] Guo, Y., Yu, C., Xiang, X., Lian, L., Shen, K., Zhong, Y., 2025. Monte Carlo-based path following precision analysis of marine vehicles with sensor measurement errors and random wave excitation. *Nonlinear Dynamics*, 113(9), 9257-9273. https://doi.org/10.1007/s11071-024-10787-5

[32] Kobayashi, R., and Okada, S., 2016. Development of hovering control system for an underwater vehicle to perform core internal inspections. *Journal of Nuclear Science and Technology*, 53(4), 566-573. https://doi.org/10.1080/00223131.2015.1064331

[33] Zhang, G., Xia, X., Guo, J., 2024. Configuration synthesis and grasping performance analysis of multi-loop coupling capture mechanism for launch and recovery of torpedo-shaped autonomous underwater vehicle. *China Ocean Engineering*, 38(3), 453-466. https://doi.org/10.1007/s13344-024-0036-8